nature nanotechnology

LETTERS

PUBLISHED ONLINE: 11 AUGUST 2013 | DOI: 10.1038/NNANO.2013.151

Optical generation of excitonic valley coherence in monolayer WSe_2

Aaron M. Jones[1], Hongyi Yu[2], Nirmal J. Ghimire[3,4], Sanfeng Wu[1], Grant Aivazian[1], Jason S. Ross[5], Bo Zhao[1], Jiaqiang Yan[4,6], David G. Mandrus[3,4,6], Di Xiao[7], Wang Yao[2]* and Xiaodong Xu[1,5]*

As a consequence of degeneracies arising from crystal symmetries, it is possible for electron states at band-edges ('valleys') to have additional spin-like quantum numbers[1–6]. An important question is whether coherent manipulation can be performed on such valley pseudospins, analogous to that implemented using true spin, in the quest for quantum technologies[7,8]. Here, we show that valley coherence can be generated and detected. Because excitons in a single valley emit circularly polarized photons, linear polarization can only be generated through recombination of an exciton in a coherent superposition of the two valley states. Using monolayer semiconductor WSe_2 devices, we first establish the circularly polarized optical selection rules for addressing individual valley excitons and trions. We then demonstrate coherence between valley excitons through the observation of linearly polarized luminescence, whose orientation coincides with that of the linearly polarized excitation, for any given polarization angle. In contrast, the corresponding photoluminescence from trions is not observed to be linearly polarized, consistent with the expectation that the emitted photon polarization is entangled with valley pseudospin. The ability to address coherence[9,10], in addition to valley polarization[11–15], is a step forward towards achieving quantum manipulation of the valley index necessary for coherent valleytronics.

Monolayer group VI transition-metal dichalcogenides are recently discovered two-dimensional semiconductors[16]. They have a direct bandgap in the visible range, with the band-edge located at energy degenerate valleys ($\pm$K) at the corners of the hexagonal Brillouin zone[17,18]. Initial experiments have demonstrated the formation of highly stable neutral and charged excitons in these monolayer semiconductors, where optically excited electrons and holes are bound together by strong Coulomb interactions[19,20]. In conventional semiconductors, such as GaAs, excitons and trions form at the Brillouin zone centre. However, in monolayer transition-metal dichalcogenides, confinement of electrons and holes to the $\pm$K valleys gives rise to valley excitons and trions, formed at an energy-degenerate set of non-central points in momentum space.

In principle, these valley excitons offer unprecedented opportunities to dynamically manipulate valley index using optical means, as has been done for optically driven spintronics. Previous work has shown that the structural inversion asymmetry present in monolayer transition-metal dichalcogenides gives rise to valley-dependent circularly polarized optical selection rules using the single particle picture[1,11]. Recent observations and electrical control of polarized photoluminescence in atomically thin molybdenum disulphide are important steps towards the optical generation and detection of valley polarization[11–15]. A more challenging but conceptually appealing possibility is to realize quantum coherence between the two well-separated band extrema in momentum space, that is, valley quantum coherence, which has not been achieved in solid-state systems.

Here we investigate the generation and readout of excitonic intervalley quantum coherence in monolayer WSe_2 devices using polarization-resolved photoluminescence spectroscopy. We obtained monolayer WSe_2 by mechanical exfoliation of synthetic WSe_2 crystals onto 300 nm SiO_2 on heavily doped silicon substrates. Figure 1a presents a microscope image of a device fabricated by electron-beam lithography. We then used photoluminescence spectroscopy to investigate the valley excitonic properties in this two-dimensional system. The sample was studied at a temperature of 30 K with an excitation energy of 1.88 eV and spot size of 1.5 μm, unless otherwise specified. We also verified that the applied laser power was within the linear response regime (Supplementary Fig. S1).

Figure 1b presents a two-dimensional spatial map of integrated exciton photoluminescence intensity, which confirms the approximately uniform optical quality of the sample. Figure 1c plots the photoluminescence spectrum along the spatial line cut indicated in Fig. 1b, and clearly shows two pronounced excitonic emission features at 1.71 and 1.74 eV. We identified that these two highest-energy excitonic emissions are associated with the A exciton[21] by comparing the differential reflection spectrum (black curve, Fig. 1d) with the photoluminescence spectrum[12,19,22] (red curve, Fig. 1d). These sharp and well-separated excitonic features are in clear contrast with the broad spectral width of photoluminescence emission in monolayer MoS_2[11–13,17,18], but are comparable with recent observations in monolayer $MoSe_2$ (ref. 19).

We assigned the exciton species by monitoring the photoluminescence emission as a function of gate voltage V_g, which controls the monolayer carrier density. Figure 2a shows the photoluminescence map versus photon energy and V_g. The spectral features below 1.675 eV probably arise from phonon side bands, which are gate-tunable; these are not discussed here. When V_g is near zero, this monolayer semiconductor is approximately intrinsic, and neutral exciton (X^o) emission at 1.749 eV dominates. By either increasing or decreasing V_g, excess electrons or holes are injected into the monolayer. X^o tends to capture an extra carrier to form a bounded three-particle system (trion) with smaller emission

[1]Department of Physics, University of Washington, Seattle, Washington 98195, USA, [2]Department of Physics and Center of Theoretical and Computational Physics, University of Hong Kong, Hong Kong, China, [3]Department of Physics and Astronomy, University of Tennessee, Knoxville, Tennessee 37996, USA, [4]Materials Science and Technology Division, Oak Ridge National Laboratory, Oak Ridge, Tennessee 37831, USA, [5]Department of Materials Science and Engineering, University of Washington, Seattle, Washington 98195, USA, [6]Department of Materials Science and Engineering, University of Tennessee, Knoxville, Tennessee 37996, USA, [7]Department of Physics, Carnegie Mellon University, Pittsburgh, Pennsylvania 15213, USA.
*e-mail: wangyao@hku.hk; xuxd@uw.edu

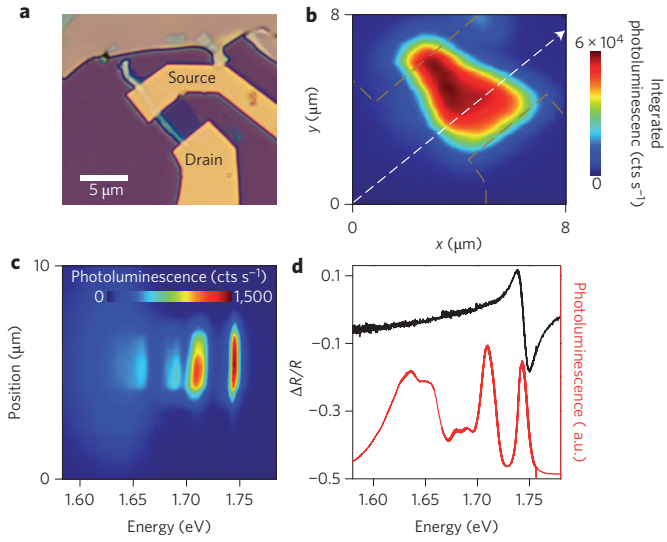

Figure 1 | Device and photoluminescence characterization. a, Optical microscope image of a monolayer WSe_2 field-effect transistor. **b**, Spatial map of integrated exciton photoluminescence of the device in **a** at $V_g = 0$ V. Gold dashed lines indicate source and drain electrodes. **c**, Photoluminescence intensity map as a function of position and photon energy along the line cut in **b**. **d**, Comparison of differential reflection (black curve) and photoluminescence (red curve) spectra for monolayer WSe_2. Data were taken before device fabrication.

energy[23]. The data demonstrate that we can either obtain X^+ (two holes and one electron) at negative V_g or X^- (two electrons and one hole) at positive V_g (ref. 19).

At V_g larger than 20 V, a photoluminescence feature ($X^{-\prime}$) emerges on the low-energy side of X^- and dominates the spectrum as V_g (electron concentration) continues to increase. As a function of V_g, the photoluminescence intensity, shift in binding energy (Fig. 2b, inset), differential reflection spectrum (Supplementary Fig. S2) and polarization dependence (presented below) show that $X^{-\prime}$ behaves in the same way as X^- and thus probably arises from the fine structure of X^-. Figure 2b plots the peak intensity of X^o, X^+, X^- and $X^{-\prime}$ as a function of V_g, and clearly shows the gate-tunable excitonic emission.

The binding energy of trions can be directly extracted by taking the energy difference between the trion and neutral exciton in Fig. 2a. Because of the true two-dimensional nature and large effective mass of the carriers, the binding energies of trions in monolayer WSe_2 are much greater than in quasi two-dimensional systems[19,20]. Within the applied voltage range, the binding energy of X^+ varies from 24 meV near $V_g = 0$ to 30 meV near $V_g = -60$ V, while that of X^- changes from 30 meV to 40 meV over a range of 45 V (Fig. 2b, inset). Because the peak position of X^o is nearly independent of V_g while trions redshift, the significant tuning of trion binding energies as a function of V_g is most probably a result of the quantum-confined Stark effect[24].

We now turn to the investigation of valley exciton polarization. Figure 3a shows the polarization-resolved photoluminescence spectra at selected gate voltages under σ^+ light excitation. The complete data set, including all V_g and σ^- excitation, can be found in Supplementary Figs S3 and S4. The data show that the photoluminescence of X^+, X^o, X^- and $X^{-\prime}$ are all highly circularly polarized. This observation demonstrates that valley optical selection rules[1] derived from the single particle picture are inherited by both neutral and charged excitonic states. It is thus feasible to selectively address valley degrees of freedom through these sharp and well-separated exciton species by using circularly polarized optical fields. The ground-state configurations for valley excitons and trions and their optical selection rules are shown schematically in Fig. 3b.

We also investigated the polarization of valley excitons as a function of photoexcitation energy. Figure 3c shows the polarization-resolved photoluminescence spectra with σ^+ excitation for different photon energies. We define the photoluminescence polarization as $\rho = \big(\mathrm{PL}(\sigma^+) - \mathrm{PL}(\sigma^-)\big)/\big(\mathrm{PL}(\sigma^+) + \mathrm{PL}(\sigma^-)\big)$ where $\mathrm{PL}(\sigma^\pm)$ is the detected photoluminescence intensity for polarization $\sigma^\pm$. Figure 3d plots the peak polarization of X^+ (yellow star), X^- (red circle), X^o (black triangle) and $X^{-\prime}$ (blue square) as a function of photoexcitation energy. The data show that ρ does not decrease significantly as photoexcitation energy increases from 1.79 eV to 2.33 eV, ~80 times the exciton linewidth above the valley exciton emission energy. This remarkable observation is distinct from the previous valley polarization reported in monolayer MoS_2 (refs 11–13), where valley polarization was generated only when the photoexcitation energy was within the linewidth of the exciton emission. Our observation suggests that these neutral and charged valley excitons have robust optical selection rules within a large neighbourhood of the K point in the Brillouin zone[11], and that interactions during hot-carrier relaxation are not the main mechanisms causing valley depolarization.

The most significant finding is that for linearly polarized light excitation, X^o emission is also highly linearly polarized ($\rho = 0.4$),

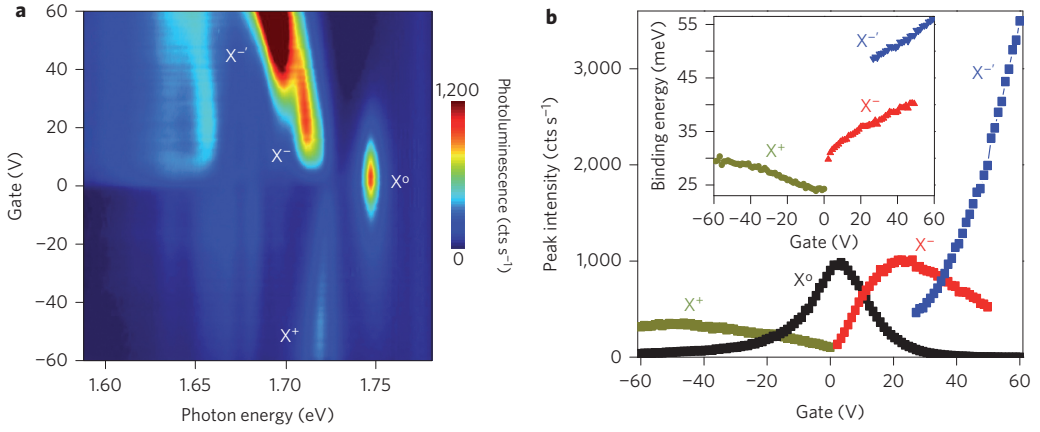

Figure 2 | Electrical control of valley excitons. a, Photoluminescence intensity map as a function of gate voltage and photon energy showing neutral exciton (X^o), negative trion (X^-) and its fine structure ($X^{-\prime}$), and positive trion (X^+) states. **b**, Peak intensity of exciton and trion photoluminescence as a function of gate voltage. Inset: trion binding energy as a function of gate voltage.

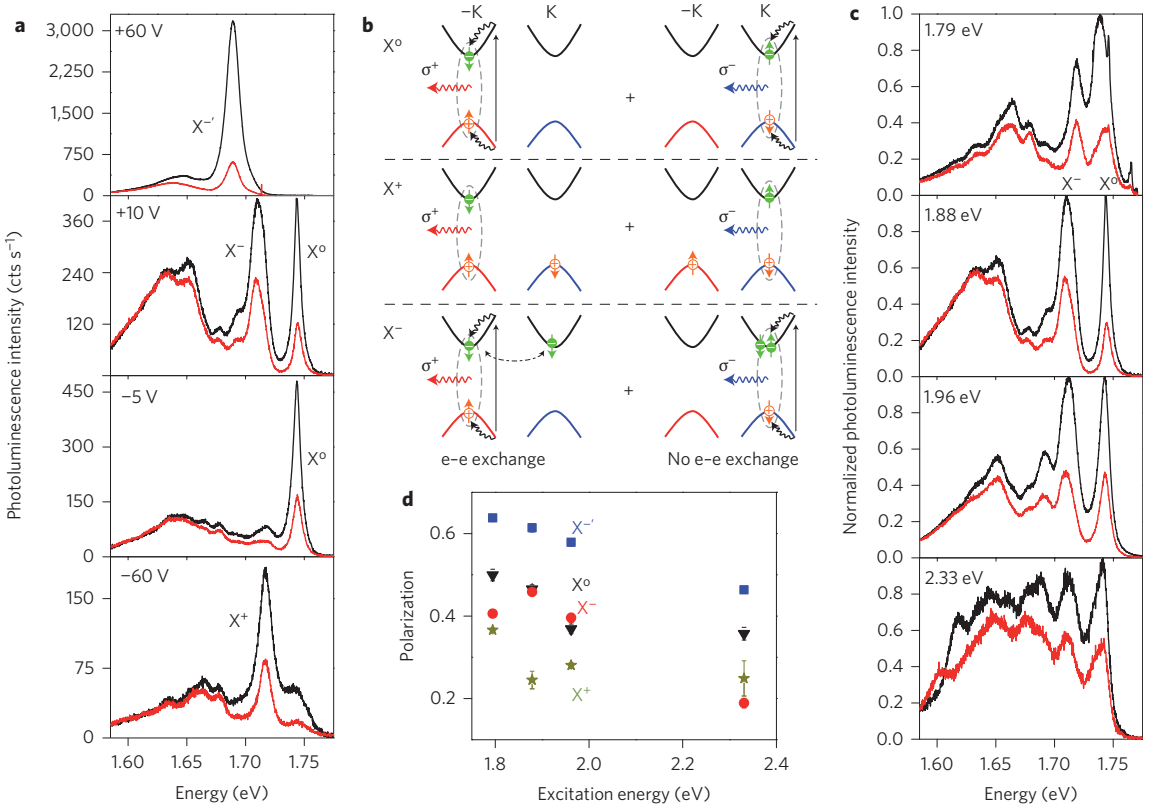

Figure 3 | Optical generation of valley exciton and trion polarization. a, Polarization-resolved photoluminescence spectra at selected gate voltages for σ^+ (black curve) and σ^- (red curve) detection. Incident laser is σ^+ polarized. Excitonic peaks are labelled. **b**, Cartoons illustrating valley excitons, where green (orange) symbols represent electrons (holes) in the conduction (valence) band. Arrow indicates spin up or down. Optical excitation is denoted by a vertical black arrow, relaxation to the band-edge by a black wavy arrow, and emitted σ^+ (σ^-) light by red (blue) wavy arrows. Both X^o and X^+ have two valley configurations, as holes at −K (K) only have spin-up (-down) states due to giant spin-valley coupling. The emission of a σ^+ (σ^-) photon by X^+ leaves behind a spin-down (-up) hole. X^- has six possible configurations. The two X^- configurations shown here emit, respectively, a σ^+ and σ^- photon, leaving a spin-down electron in the +K valley. Their time-reversal configurations (not shown) leave a spin-up electron in the −K valley on photon emission. Electron–electron (e-e) exchange interaction is present (absent) for the configuration on the left (right), indicated by a black dash-dotted arrow. **c**, Polarization-resolved photoluminescence spectra as a function of photoexcitation energy (indicated in top left corner) for σ^+ (black curve) and σ^- (red curve) detection. Incident laser is σ^+ polarized. **d**, Degree of valley exciton and trion polarization as a function of photoexcitation energy. Error bars show the standard deviation of the polarization at the peak.

while trion photoluminescence is not. Figure 4a shows the photoluminescence spectra at selected V_g under horizontally (H) polarized light excitation at 1.88 eV (Supplementary Figs S5 and S6 show the complete data set). The data show that the H component of X^o (black curve) is much stronger than the vertically polarized (V) photoluminescence component (red curve), while trions have equal photoluminescence intensity for either H or V detection.

By investigating the linearly polarized photoluminescence for arbitrarily oriented linearly polarized excitation, we found that the observed X^o polarization is independent of crystal orientation. Figure 4b shows polar plots of X^o peak intensity as a function of detection angle for a given incident linear polarization angle θ. The blue lines are fits using $r = A \times (1 + \rho \times \cos\ 2[x - \varphi])$ where A is a normalization constant, x is the angle of detection and φ is the X^o polarization angle. We extract φ and plot it as a function of θ in Fig. 4c, which is fit well by a line with a slope of unity. The data demonstrate that φ is completely determined by θ, and ρ is isotropic (red squares in Fig. 4c). Linearly polarized X^o emission has been observed in other solid-state systems. For example, crystal anisotropy will lead to linearly polarized exciton emission with the polarization axis predetermined by the axis of anisotropy[25–27]. In systems that lack crystal anisotropy, the isotropic linear polarization can be generated if excitonic coherence is maintained for longer than the exciton recombination time[28–31].

Because monolayer WSe_2 has three-fold rotational symmetry, we attribute the above finding to the generation of excitonic quantum coherence between opposite valleys by linearly polarized light. We have shown that with σ^+ (σ^-) polarized laser excitation, X^o is highly polarized at the −K (+K) valley by the circularly polarized valley optical selection rule (Fig. 3b). Because linear polarization is a coherent superposition of σ^+ and σ^-, it will simultaneously excite both −K and +K valleys and transfer the optical coherence to valley quantum coherence; that is, the photoexcited electron–hole pair is a linear superposition in the valley subspace,

$$\sum_{\mathbf{q}} a(\mathbf{q}) \left(e^{-i\theta} \hat{e}^{+}_{-\mathbf{K}+\frac{\mathbf{q}}{2},\downarrow} \hat{h}^{+}_{\mathbf{K}-\frac{\mathbf{q}}{2},\Uparrow} + e^{+i\theta} \hat{e}^{+}_{\mathbf{K}+\frac{\mathbf{q}}{2},\uparrow} \hat{h}^{+}_{-\mathbf{K}-\frac{\mathbf{q}}{2},\Downarrow} \right) |\Phi\rangle$$

Here $a(\mathbf{q})$ is the linear superposition expansion coefficient, $\mathbf{q}$ is the wave vector measured from the K points, $|\Phi\rangle$ is the vacuum state with empty conduction bands and fully filled valence bands, $\hat{e}^{+}_{\mathbf{k},\downarrow}$ creates a spin-down electron in the conduction band, and $\hat{h}^{+}_{-\mathbf{k},\Uparrow}$ corresponds to the creation of a spin-up hole with momentum $-\mathbf{k}$ in the valence band (annihilation of a spin-down electron with crystal momentum $\mathbf{k}$). The observation of linearly polarized X^o photoluminescence parallel to the arbitrarily oriented linearly polarized excitation implies that the intervalley coherence has been preserved in the exciton formation.

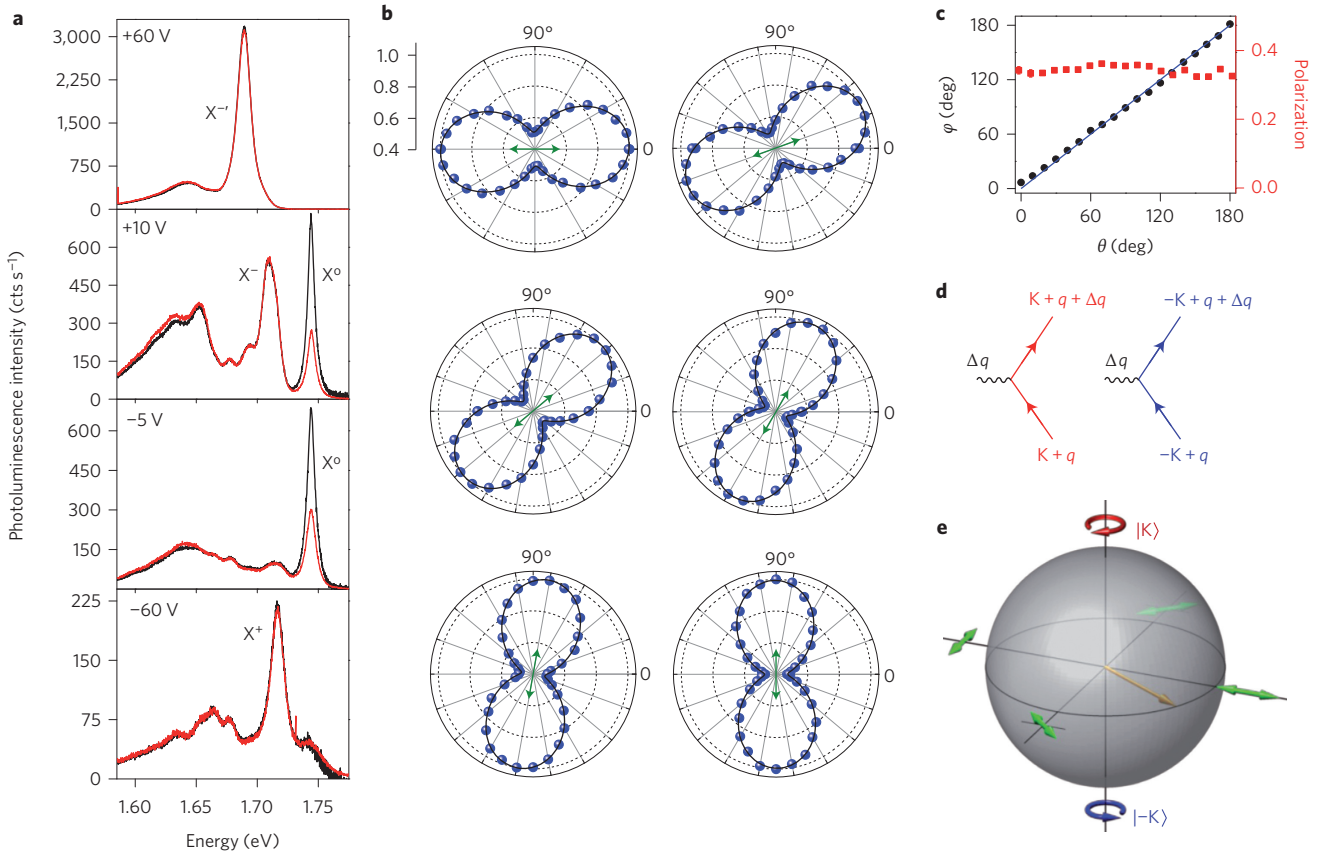

Figure 4 | Signature of excitonic valley quantum coherence. a, Polarization-resolved photoluminescence spectra at selected gate voltages for horizontally (H, black curve) and vertically (V, red curve) polarized detection. Incident laser is horizontally polarized. **b**, Normalized neutral exciton peak intensity, *r*, as a function of detection angle for given incident laser polarization (marked by green arrow). 0.4 corresponds to the centre and 1.0 to the outermost dashed circle. **c**, Polarization axis φ (black dots) and degree of linear polarization (red squares) of neutral exciton photoluminescence as a function of incident linear polarization angle θ. Blue line is a linear fit with a slope of unity. **d**, Intravalley scattering Feynman diagram. The wavy line denotes the Fourier component (with wave vector $\Delta q \ll 2\mathrm{K}$) of the effective scattering potential by an impurity, phonon or the Coulomb interaction from other carriers. As the effective scattering potential is identical for valleys K and −K, the corresponding quantum trajectories for carriers in states $|\mathrm{K},q\rangle$ and $|-\mathrm{K},q\rangle$ are equivalent, and the relative phase in the valley subspace remains unchanged. **e**, Bloch sphere representation of optical manipulation of excitonic valley pseudo-spins. North and south poles correspond to valleys K and −K, respectively, where emitted photoluminescence is circularly polarized. State vectors at the equator (orange arrow) are a coherent superposition of the two valleys, corresponding to linearly polarized photoluminescence. The photoluminescence polarization direction is indicated by arrows outside the sphere.

Key to the preservation of valley quantum coherence is the equivalence of quantum trajectories for the photoexcited electron (hole) on states $|\mathbf{K}+\mathbf{q}\rangle$ and $|-\mathbf{K}+\mathbf{q}\rangle$ so that their relative phase remains unchanged in exciton formation. As the exciton emission is at ~1.75 eV, we infer that the 1.88 eV excitation energy is below the electron–hole continuum because the exciton binding energy in monolayer transition-metal dichalcogenides is on the order of 0.3–0.5 eV (refs 19,20). Exciton formation mechanisms include the Coulomb interaction with other carriers and coupling to phonons to transfer the binding energy[32]. The former is dominated by intravalley scattering because of the large momentum space separation between valleys and the long-range nature of the Coulomb interaction. The intravalley Coulomb interaction is independent of the valley index and preserves both the valley polarization and valley coherence (Supplementary Section S1, Fig. S7). Exciton formation through phonon-assisted intravalley scattering also preserves valley polarization and coherence, as such processes are also valley-independent (Fig. 4d).

The above physical picture is also consistent with the absence of linear polarization for trion emission. For the X^+ trion, there are only two possible configurations, as shown in Fig. 3b, because the holes at the valley +K (−K) only have spin-down (-up) states due to the giant spin–valley coupling and time-reversal symmetry[1]. Upon electron–hole recombination, one X^+ configuration becomes a σ^+ photon plus a spin-down hole, and the other becomes a σ^- photon plus a spin-up hole. Their linear superposition can only lead to a spin–photon entanglement: $e^{-i\theta}|\sigma^+\rangle|\Downarrow\rangle + e^{i\theta}|\sigma^-\rangle|\Uparrow\rangle$. Linearly polarized photons as a superposition of σ^+ and σ^- are always forbidden for X^+ emission, because the hole states associated with σ^+ and σ^- are orthogonal.

For the X^- trion, although the number of possible configurations is tripled (Supplementary Fig. S8) as electrons in each valley have both spin-up and spin-down states, only the linear combination of the two configurations shown in Fig. 3b (and the time reversal of this combination) can in principle emit a linearly polarized photon. However, we found that the Coulomb exchange interaction leads to a fine splitting between these two X^- trion configurations. This exchange interaction will probably destroy the valley coherence created by linearly polarized excitation (Supplementary Section S2), resulting in the absence of linearly polarized photoluminescence for X^-. Thus, our observation of linearly polarized excitons but not trions strongly indicates the optical generation of excitonic valley quantum coherence.

We introduce the Bloch sphere (Fig. 4e) to summarize our work on the optical manipulation of valley pseudo-spins through valley excitons and trions. Circularly polarized light prepares valley pseudo-spin on the north (+K) or south (−K) pole, while arbitrary linearly polarized light prepares states on the equator as a coherent superposition of +K and −K valleys. In principle, states on the Bloch sphere away from the poles and equator can be created by elliptically polarized light excitation. Our demonstration of optical generation of valley coherence shows a viable way to manipulate valley degrees of freedom in a coherent manner, akin to the manipulation of electron spins for coherent spintronics, and potentially leading to optically driven coherent valleytronics in a solid-state system.

The observed degree of polarization of X^o for circular and linear excitation implies that both the longitudinal and transverse decoherence times of the exciton valley pseudospin are comparable to or even slower than the electron–hole recombination time. Possible mechanisms of valley decoherence include intervalley scattering of carriers by the Coulomb interaction and phonons. In addition, the electron–hole exchange interaction in an exciton can give rise to an effective coupling between its valley pseudospin and its centre-of-mass motion, which causes valley decoherence[33] (Supplementary Section S1). We hope that our work will stimulate both experimental and theoretical investigations of exciton scattering and interactions in monolayer semiconductors, to further reveal the mechanisms and timescales related to valley decoherence.

Received 13 March 2013; accepted 8 July 2013;
published online 11 August 2013

References

1. Xiao, D., Liu, G-B., Feng, W., Xu, X. & Yao, W. Coupled spin and valley physics in monolayers of MoS_2 and other group-VI dichalcogenides. *Phys. Rev. Lett.* **108,** 196802 (2012).
2. Zhu, Z., Collaudin, A., Fauque, B., Kang, W. & Behnia, K. Field-induced polarization of Dirac valleys in bismuth. *Nature Phys.* **8,** 89–94 (2012).
3. Rycerz, A., Tworzydlo, J. & Beenakker, C. W. J. Valley filter and valley valve in graphene. *Nature Phys.* **3,** 172–175 (2007).
4. Bishop, N. C. *et al.* Valley polarization and susceptibility of composite fermions around a filling factor $\nu = 3/2$. *Phys. Rev. Lett.* **98,** 266404 (2007).
5. Gunawan, O. *et al.* Valley susceptibility of an interacting two-dimensional electron system. *Phys. Rev. Lett.* **97,** 186404 (2006).
6. Gunawan, O., Habib, B., De Poortere, E. P. & Shayegan, M. Quantized conductance in an AlAs two-dimensional electron system quantum point contact. *Phys. Rev. B* **74,** 155436 (2006).
7. Gupta, J. A., Knobel, R., Samarth, N. & Awschalom, D. D. Ultrafast manipulation of electron spin coherence. *Science* **292,** 2458–2461 (2001).
8. Press, D., Ladd, T. D., Zhang, B. & Yamamoto, Y. Complete quantum control of a single quantum dot spin using ultrafast optical pulses. *Nature* **456,** 218–221 (2008).
9. Laird, E. A., Pei, F. & Kouwenhoven, L. P. A valley–spin qubit in a carbon nanotube. Preprint at http://lanl.arXiv.org/1210.3085 (2012).
10. Pályi, A. & Burkard, G. Disorder-mediated electron valley resonance in carbon nanotube quantum dots. *Phys. Rev. Lett.* **106,** 086801 (2011).
11. Cao, T. *et al.* Valley-selective circular dichroism of monolayer molybdenum disulphide. *Nature Commun.* **3,** 887 (2012).
12. Mak, K. F., He, K., Shan, J. & Heinz, T. F. Control of valley polarization in monolayer MoS_2 by optical helicity. *Nature Nanotech.* **7,** 494–498 (2012).
13. Zeng, H., Dai, J., Yao, W., Xiao, D. & Cui, X. Valley polarization in MoS_2 monolayers by optical pumping. *Nature Nanotech.* **7,** 490–493 (2012).
14. Sallen, G. *et al.* Robust optical emission polarization in MoS_2 monolayers through selective valley excitation. *Phys. Rev. B* **86,** 081301 (2012).
15. Wu, S. *et al.* Electrical tuning of valley magnetic moment through symmetry control in bilayer MoS_2. *Nature Phys.* **9,** 149–153 (2013).
16. Novoselov, K. S. *et al.* Two-dimensional atomic crystals. *Proc. Natl Acad. Sci. USA* **102,** 10451–10453 (2005).
17. Mak, K. F., Lee, C., Hone, J., Shan, J. & Heinz, T. F. Atomically thin MoS_2: a new direct-gap semiconductor. *Phys. Rev. Lett.* **105,** 136805 (2010).
18. Splendiani, A. *et al.* Emerging photoluminescence in monolayer MoS_2. *Nano Lett.* **10,** 1271–1275 (2010).
19. Ross, J. S. *et al.* Electrical control of neutral and charged excitons in a monolayer semiconductor. *Nature Commun.* **4,** 1474 (2013).
20. Mak, K. F. *et al.* Tightly bound trions in monolayer MoS_2. *Nature Mater.* **12,** 207–211 (2013).
21. Coehoorn, R., Haas, C. & de Groot, R. A. Electronic structure of $MoSe_2$, MoS_2, and WSe_2. II. The nature of the optical band gaps. *Phys. Rev. B* **35,** 6203–6206 (1987).
22. Zhao, W. *et al.* Evolution of electronic structure in atomically thin sheets of WS_2 and WSe_2. *ACS Nano* **7,** 791–797 (2013).
23. Kheng, K. *et al.* Observation of negatively charged excitons X^- in semiconductor quantum wells. *Phys. Rev. Lett.* **71,** 1752–1755 (1993).
24. Miller, D. A. B. *et al.* Band-edge electroabsorption in quantum well structures: the quantum-confined Stark effect. *Phys. Rev. Lett.* **53,** 2173–2176 (1984).
25. Misewich, J. A. *et al.* Electrically induced optical emission from a carbon nanotube FET. *Science* **300,** 783–786 (2003).
26. Lefebvre, J., Fraser, J. M., Finnie, P. & Homma, Y. Photoluminescence from an individual single-walled carbon nanotube. *Phys. Rev. B* **69,** 075403 (2004).
27. Bayer, M. *et al.* Electron and hole *g* factors and exchange interaction from studies of the exciton fine structure in $In_{0.6}Ga_{0.4}As$ quantum dots. *Phys. Rev. Lett.* **82,** 1748–1751 (1999).
28. Bonnot, A., Planel, R. & à la Guillaume, C. B. Optical orientation of excitons in CdS. *Phys. Rev. B* **9,** 690–702 (1974).
29. Amand, T. *et al.* Spin quantum beats of 2D excitons. *Phys. Rev. Lett.* **78,** 1355–1358 (1997).
30. Mohan, A. *et al.* Polarization-entangled photons produced with high-symmetry site-controlled quantum dots. *Nature Photon.* **4,** 302–306 (2010).
31. Dousse, A. *et al.* Ultrabright source of entangled photon pairs. *Nature* **466,** 217–220 (2010).
32. Gibbs, H. M., Khitrova, G. & Koch, S. W. Exciton–polariton light–semiconductor coupling effects. *Nature Photon.* **5,** 273–273 (2011).
33. Maialle, M. Z., de Andrada e Silva, E. A. & Sham, L. J. Exciton spin dynamics in quantum wells. *Phys. Rev. B* **47,** 15776–15788 (1993).

Acknowledgements

The authors thank B. Spivak, D. Cobden, A. Andreev and K-M. Fu for helpful discussions. This work was mainly supported by the National Science Foundation (NSF, DMR-1150719). The experimental set-up and device fabrication was partially supported by a Defense Advanced Research Projects Agency (DARPA) Young Faculty Award (YFA) (N66001-11-1-4124). H.Y. and W.Y. were supported by the Research Grant Council (HKU705513P) and the University Grant Council (AoE/P-04/08) of the government of Hong Kong, and the Croucher Foundation under the Croucher Innovation Award. N.G., J.Y., D.M. and D.X. were supported by the US Department of Energy (DoE), Basic Energy Sciences (BES), Materials Sciences and Engineering Division. Device fabrication was performed at the University of Washington Microfabrication Facility and the NSF-funded Nanotech User Facility.

Author contributions

X.X. conceived the experiments. A.M.J. performed the experiments, assisted by S.W., G.A. and B.Z. The devices were fabricated by J.S.R., assisted by A.M.J. The theoretical explanation was provided by H.Y. and W.Y., with input from D.X. The WSe_2 crystals were synthesized by N.J.G., J.Y. and D.G.M., who also performed bulk characterization measurements. A.M.J., X.X., H.Y. and W.Y. co-wrote the paper. All authors discussed the results and commented on the manuscript.

Additional information

Supplementary information is available in the online version of the paper. Reprints and permissions information is available online at www.nature.com/reprints. Correspondence and requests for materials should be addressed to W.Y. and X.X.

Competing financial interests

The authors declare no competing financial interests.